Journal of Geophysical Research: Atmospheres

RESEARCH ARTICLE
10.1029/2017JD028083

Under What Conditions Can We Trust Retrieved Cloud Drop Concentrations in Broken Marine Stratocumulus?

Yannian Zhu[1,2], **Daniel Rosenfeld**[3], **and Zhanqing Li**[1,4]

[1]State Laboratory of Earth Surface Process and Resource Ecology, College of Global Change and Earth System Science, Beijing Normal University, Beijing, China, [2]Meteorological Institute of Shaanxi Province, Xi'an, China, [3]Institute of Earth Sciences, The Hebrew University of Jerusalem, Jerusalem, Israel, [4]Department of Atmospheric and Oceanic Science and Earth System Science Interdisciplinary Center, University of Maryland, College Park, MD, USA

Key Points:
- The brightest 10% of cloudy pixels likely best represent cloud cores where N_d retrieval assumptions are best met
- The criterion is representative of pixels that are also fully surrounded by cloudy pixels (N_d agreement within 5%)
- The retrieved drop concentrations likely best reflect the aerosol and updraft effects on cloud properties

Correspondence to:
Z. Li,
zli@atmos.umd.edu

Citation:
Zhu, Y., Rosenfeld, D., & Li, Z. (2018). Under what conditions can we trust retrieved cloud drop concentrations in broken marine stratocumulus? *Journal of Geophysical Research: Atmospheres*, *123*, 8754–8767. https://doi.org/10.1029/2017JD028083

Received 24 NOV 2017
Accepted 10 JUL 2018
Accepted article online 20 JUL 2018
Published online 16 AUG 2018

Abstract In this study, we show how to obtain more reliable satellite-retrieved cloud drop number concentrations (N_d) from Moderate Resolution Imaging Spectroradiometer (MODIS) standard cloud products. N_d is important as a fundamental cloud property that determines cloud albedo, precipitation-forming processes, cloud longevity, and fractional cover, all of which determine cloud radiative effects. N_d is determined by cloud base aerosols and updrafts. Satellite retrievals of N_d for marine stratocumulus clouds are performed based on the assumption of a nearly adiabatic cloud column. The retrievals, however, are fraught with problems that cause large biases (e.g., the retrieved N_d for partially filled cloudy pixels are less than one third of the retrieved N_d for the convective cores) and limit the usefulness of N_d, especially in broken cloud fields. The N_d of the brightest 10% of cloudy pixels are selected because the brightest clouds are the convective cores that most closely follow adiabatic parcels, a key assumption of our retrieval. It is shown that this criterion is representative of pixels that are also fully surrounded by cloudy pixels (N_d agreement within 5%).

1. Background

The cloud drop number concentration (N_d) is a fundamental cloud property that controls the cloud drop effective radius (r_e) for a given amount of cloud water content. In turn, r_e determines the coalescence rate, which is approximately proportional to r_e^5 (Freud & Rosenfeld, 2012). The dynamic response of a cloud system to the formation of precipitation greatly affects its organization, cloud cover, and radiative properties (Albrecht, 1989; Goren & Rosenfeld, 2015). Marine stratocumulus decks often break up when precipitating more than ~2 mm/day (Rosenfeld et al., 2006, 2012) with differences in cloud radiative effects that can exceed 100 W/m^2 (Goren & Rosenfeld, 2014). Here the radiative effect is defined as the difference in solar-reflected radiation between cloudy and cloud-free situations at the same time and place. Since N_d is determined by both cloud base updrafts (W_b) and cloud condensation nuclei (CCN) for a given cloud base pressure and temperature (Pinsky et al., 2012), the emerging capability of retrieving both N_d and W_b of convective clouds from satellite data makes it possible to retrieve CCN and cloud base supersaturation (Rosenfeld et al., 2016; Zheng et al., 2016).

Satellite-retrieved CCN based on retrieved W_b and N_d aims at replacing the satellite-retrieved aerosol optical depth (AOD) as a proxy for CCN. Climate studies addressing cloud-aerosol interactions have mostly related AOD to cloud properties and radiative effects (e.g., Quaas et al., 2010). However, AOD is poorly related to CCN, especially at low concentrations (e.g., CCN 100#/cm^3) that are typical of pristine marine boundary layer (Andreae, 2009; Stier, 2016). In fact, the optical signal of CCN $<$ 100–150#/cm^3 is below the discernible optical signal of AOD by both passive (Shinozuka et al., 2015) and lidar (Zamora et al., 2017) satellite measurements.

Using satellite-retrieved CCN based on the retrieved W_b and N_d may overcome many of the limitations of using AOD for quantifying cloud-aerosol interactions.

The N_d retrieval should reflect CCN and updrafts at the base of convective cloud elements, so we focus on those cloud elements that constitute the convective cores of cloud fields. These cores have the highest updrafts and liquid water paths (LWPs), and resemble adiabatic clouds the closest. Therefore, this study makes an effort to focus on these elements in the context of marine stratocumulus.

Table 1
List of Notations and Abbreviations

Abbreviations	Parameters
CF	Cloud fraction (unitless)
CCN	Cloud condensation nuclei (cm^{-3})
LWC	Cloud liquid water path (g/m^3)
LWP	Cloud liquid water content (g/m^2)
N_d	Cloud drop concentrations (cm^{-3})
$N_{d\_average}$	Average N_d for pixels with an r_e uncertainty less than 10%
N_{d50}	Average N_d for pixels with τ_{50} (cm^{-3})
N_{d90}	Average N_d for pixels with τ_{90} (cm^{-3})
$N_{d90\_embedded}$	Average N_d for pixels embedded with other cloudy pixels having τ_{90} (cm^{-3})
$N_{d\_high\_uncertainty}$	Average N_d for pixels with an r_e uncertainty greater than 10%
r_e	Cloud drop effective radius (μm)
r_v	Cloud drop volume radius (μm)
W_b	Cloud-base updrafts (m/s)
τ	Cloud optical thickness (unitless)
τ_{50}	Scene-computed τ for pixels with τ larger than its median value (unitless)
τ_{90}	Scene-computed τ for pixels with τ larger than its 90th percentile (unitless)

Rosenfeld et al. (2016) used N_d retrieved for convective clouds based on the rate of growth of r_e with decreasing cloud top temperature (T). To resolve the small convective elements while minimizing the strong three-dimensional effects (Marshak et al., 2006), they used 3.7 μm solar reflectance at a 375 m spatial resolution and restricted to backscatter angles ±30° as measured by the Visible Infrared Imager Radiometer Suite onboard the Suomi National Polar-orbiting Partnership satellite. However, this methodology cannot be applied to marine stratocumulus clouds, which are typically too shallow (less than ~800 m) to provide a useful r_e (T) function for retrieving N_d (Rosenfeld et al., 2016). The common way of retrieving N_d in marine stratocumulus is by using r_e and cloud optical depth (Bennartz, 2007; Brenguier et al., 2000; Szczodrak et al., 2001). The cloud optical depth (τ) used in this study is at 0.86 μm. The application of this method to broken marine stratocumulus clouds is plagued with problems that are addressed in this study.

There are multiple problems in retrieving N_d. The reliability of retrieved cloud properties deteriorates with increasing solar zenith angle (SZA), especially when it is greater than 65° (Grosvenor & Wood, 2014). The main causes of retrieval errors are three-dimensional effects (Marshak et al., 2006) that are inherent to broken clouds with inhomogeneous pixel filling (Zhang et al., 2012). Cloud optical thickness (τ) is underestimated for partially filled cloud pixels, leading to positive and negative biases in the retrievals of r_e and N_d. The satellite-viewing geometry also has an impact on the retrieval of r_e (Vant-Hull et al., 2007).

The Moderate Resolution Imaging Spectroradiometer (MODIS) cloud product provides three kinds of 1-km resolution retrievals of r_e and τ, which are derived from near-infrared band (1.6, 2.1, and 3.7 μm) and visible band (0.86 μm) observations (Nakajima & King, 1990). One reason for differences between the three kinds of retrievals arises from their absorption and penetration depth into clouds. The penetration depth at 3.7 μm is smaller than at 2.1 μm and that at 2.1 μm is smaller than at 1.6 μm (Bennartz & Rausch, 2017; Platnick, 2000). This is caused by varying absorption strength, which has been exploited to retrieve vertical profiles of r_e near cloud tops (Chang & Li, 2002, 2003), which helps in the retrieval of cloud LWP and the formation of rain in overcast warm clouds (Chen et al., 2007, 2011). Three-dimensional effects (Hayes et al., 2010; Marshak et al., 2006; Wolters et al., 2010) are smaller in the more absorbing longer wavebands. This, in addition to the retrieval errors in r_e due to application of the look-up table approach (Zhang et al., 2012) to partially filled pixels, may explain the finding of Zhang and Platnick (2011) that r_e retrieved at 3.7 μm is substantially smaller than at 2.1 μm for inhomogeneous clouds such as trade wind cumulus clouds, especially when the clouds are optically thin.

The r_e of nonraining clouds increases from cloud base to top. Significant drizzle is formed when r_e at cloud top exceeds 14 μm (Andreae et al., 2004; Gerber, 1996; Rangno & Hobbs, 2005; Rosenfeld, 1999; Rosenfeld et al., 2012; Rosenfeld & Gutman, 1994; Rosenfeld & Woodley, 2003; Suzuki et al., 2010). As the drizzle drops fall from higher to lower parts of clouds, r_e near cloud tops become smaller while r_e at lower levels become larger. As a result, r_e retrieved at a wave band of deeper penetration depth (weaker absorption) results in a larger value (Chang & Li, 2002). Since a liquid-water cloud at 3.7 μm is more absorbing than at 2.1 μm, r_e closer to the cloud top is measured. In marine stratocumulus, cloud droplets at the cloud top are mostly smaller than a little deeper into the cloud because of evaporation to the overlying dry air, which results in cloud vertical inhomogeneity (Seethala & Horvath, 2010). Also, in drizzling clouds, larger drops fall from the cloud top, thus increasing the indicated r_e for a measurement that goes deeper into the cloud (2.1 μm) (Chang & Li, 2002; Nakajima et al., 2010a, 2010b; Suzuki et al., 2010). All these effects incur biases because the retrievals of r_e and τ are based on the assumption that clouds are both horizontally and vertically homogeneous within the instrument field of view, which further affects the N_d retrieval.

Satellite retrievals of N_d were previously applied to marine stratocumulus under the main assumption that the clouds were composed of nearly adiabatic elements (Bennartz, 2007; Brenguier et al., 2000). However, this is applicable only to the cores of the convective elements. The tops of the convective clouds spread as anvils

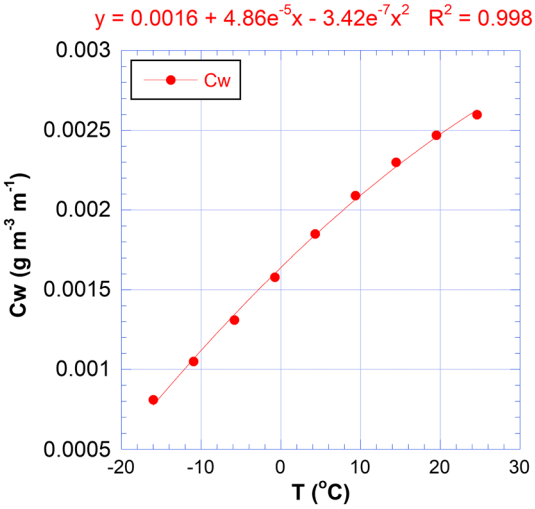

Figure 1. Condensation rate calculation.

with the inversion base. N_d retrievals outside the cores of such clouds would have large uncertainties because their properties change substantially from the cores of the convective elements as they spread, become thinner, and get more mixed with the ambient air, thus moving away from the adiabatic assumption. Painemal and Zuidema (2011) validated MODIS-derived N_d against in situ observations taken in the South Pacific during the VAMOS Ocean-Cloud-Atmosphere-Land Study (VOCALS) field campaign (Wood et al., 2011). They reported a bias of −4.0 cloud drops per cm^3 in clouds with mean adiabatic fractions of 70% that coincided with the nearly homogeneous MODIS coverage of 5 × 5 pixels. Min et al. (2012) compared satellite-retrieved N_d with in situ measurements during the VOCALS field campaign. They found that for the given domains of 5 and 25 km, the correlation coefficients were 0.91 and 0.93 with fitting slopes of 1.23 and 1.27, respectively. For adiabatic clouds only, the slopes were 1.04 and 1.07, respectively. Both results from VOCALS show that for more adiabatic clouds, the satellite-retrieved N_d is more comparable to in situ measurements. This means that the MODIS-retrieved N_d is almost bias-free in the cloud cores that best meet the adiabatic assumptions made. This is in part due the fact that the MODIS overestimate of r_e is compensated by the subadiabaticity of the clouds, even in their cores where the clouds are closest to being adiabatic. Therefore, we will focus on the cores of convective clouds that are closest to adiabatic because the retrieval of N_d relies on the premise that the deepest portions of cumulus clouds are adiabatic. This is done by assuming that the brighter parts of the clouds (e.g., τ greater than the 90th percentile of τ) represent adiabatic convective elements, which will be discussed in section 3.

Section 2 describes the data and the methodology used to calculate N_d. Quality control criteria for N_d retrievals are presented in section 3. Section 4 shows the sensitivities of N_d retrieval biases under different conditions. Section 5 examines other possible factors that may influence the N_d retrievals. The application of different N_d retrieval methods to overcast and broken cloud field cases is presented in section 6. A summary is given in section 7. For a full list of notations and abbreviations, see Table 1.

2. Retrieving N_d in Shallow Marine Clouds

We first examine MODIS retrievals of low-level water clouds over the southeastern Pacific, including marine stratocumulus in the stable boundary layer and shallow convective clouds in the unstable air during outbreaks of the polar air mass. Cloud microphysical properties at a resolution of 1 km were obtained from the MODIS collection 6 (C6) level-2 (L2) cloud product. Each MODIS granule was divided into several scenes of 110 by 110 km (1° × 1° near the equator). Each granule has 17 across-track and 18 along-track scenes, or a total of 306 scenes after removing the first and last two scenes along the across-track due to distorted pixels. For each scene, we calculate the N_d for pixels whose τ are the highest 50th or 90th percentiles by solving

$$N_d = c^{1/2}\tau^{1/2}(r_e/k)^{-5/2}, \quad (1)$$

where $c = \frac{5 \cdot A}{3 \cdot \pi \cdot Q_{ext}}$, $A = \frac{C_w}{\frac{4}{3}\pi \cdot \rho_w}$ (Szczodrak et al., 2001), and $k = 1.08$ (Freud et al., 2011) which is a parameter that relates r_e to the mean volume radius. Values for c are calculated by assuming $Q_{ext} = 2$, and the condensation rate (c_w) is calculated as follows: (a) Use a parcel model to calculate the adiabatic liquid water content at different cloud base temperatures for a given cloud base pressure, that is, 900 hPa in this study. (b) Calculate the condensed water in an air parcel that ascends 100 m starting at 100 m above cloud base. (c) Do a regression between temperature and condensed water per 100 m to calculate the c_w at different temperatures (Figure 1). The units are $g \cdot m^{-3} \cdot m^{-1}$ since it is the mass of condensed water in 1 m^3 of air mass that rises 1 m within a cloud.

3. Pixel Selection Criteria

3.1. Rejecting Pixels With High Uncertainties for r_e

Partial cloud filling of pixels causes biases when retrieving N_d. Such errors are anticipated to be larger when there are broken clouds because such clouds have greater subpixel heterogeneity. Therefore, the variability

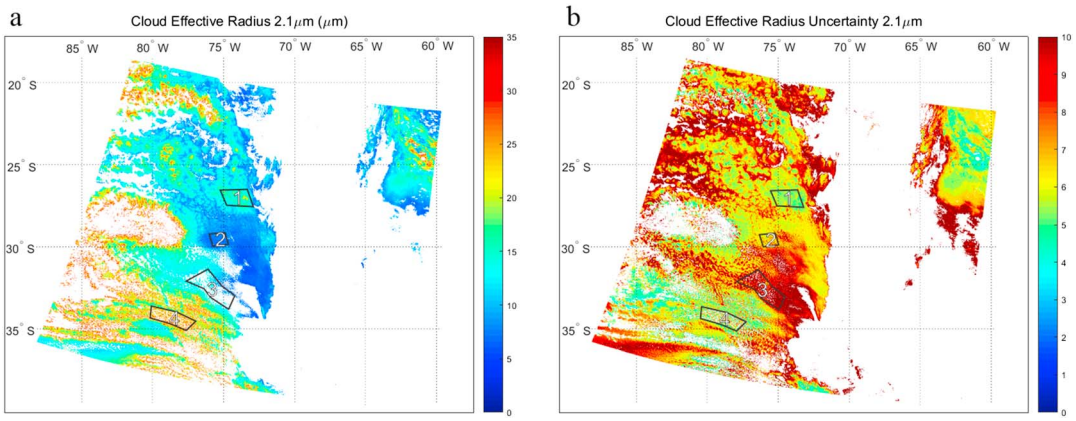

Figure 2. Left: Effective radius (μm) at 2.1 μm. Right: Cloud effective particle radius (at 2.1 μm) relative uncertainty (%). The four target scenes are outlined in black in both panels.

of the sixteen 250-m subpixels within each 1-km MODIS pixel, a parameter in the MODIS L2 cloud product, is the main criterion for determining the uncertainty of r_e (Platnick et al., 2004, 2015). For C6, the uncertainty comes from four sources: (1) instrument calibration, (2) atmospheric corrections, (3) surface spectral reflectance, and (4) other forward model error sources, but does not include uncertainties from subpixel heterogeneity or 3-D radiative effects, which can be very large, likely larger than the MODIS product uncertainties (Marshak et al., 2006; Zhang et al., 2012). As Figure 2 shows, we chose four target scenes: (1) overcast clouds with small r_e, (2) overcast clouds with large r_e, (3) broken clouds with small r_e, and (4) broken clouds with large r_e. Figure 2 shows retrievals of the MODIS r_e product and its uncertainty for these scenes, numbered by the order described here. The retrievals in broken clouds have larger relative uncertainties than in overcast clouds. Previous studies have shown that the retrieved r_e can be overestimated in thin and broken clouds due to surface contamination (Coakley Jr et al., 2005), but these effects diminish in nonbroken clouds with τ greater than ~8 in the visible (0.5 μm; Rosenfeld et al., 2004).

Figure 3 shows that the r_e of thin broken clouds has the largest uncertainty, which never exceeds 10% when τ is greater than 8. Therefore, we filter out pixels with uncertainties in r_e greater than 10%.

3.2. Focusing on Convective Cores

For each 110 km × 110 km scene, N_d was averaged using cloudy pixels with τ greater than the median of τ and cloudy pixels with τ greater than the 90th percentile of τ, denoted as N_{d50} and N_{d90}. A smaller difference between the 50th and 90th percentiles indicates clouds that are more homogeneous. However, for inhomogeneous clouds, such as clouds with tops spreading as anvils at an inversion base (see Figure 4), N_d of the different percentiles varies greatly. Therefore, we select only the brightest clouds (i.e., the optically thickest parts of the clouds) that reside within the convective cores as illustrated in Figure 4. The 90th percentile of τ already achieves that. Choosing a much higher percentile might amplify artifacts due to nonhomogeneity of the solar illuminations of the topography of cloud tops. N_d is constant and the drop size increases adiabatically in the convective cores of stratocumulus clouds (Pawlowska et al., 2000), so liquid water content increases toward the cloud tops.

3.3. Selecting Only Water Clouds

The MODIS C6 L2 cloud product provides two kinds of 1-km cloud phase product derived from two approaches. One algorithm uses infrared (IR) channels (Baum et al., 2000, 2012) for both daytime and nighttime. The other algorithm is a daytime-only shortwave-derived cloud thermodynamic phase algorithm that uses a combination of visible, shortwave IR, and IR channels. This shortwave-derived cloud phase algorithm has been refined and validated extensively against Cloud-Aerosol Lidar with Orthogonal Polarization Lidar retrievals (Marchant et al., 2016). The latter cloud phase product was used for selecting scenes with only liquid-water clouds.

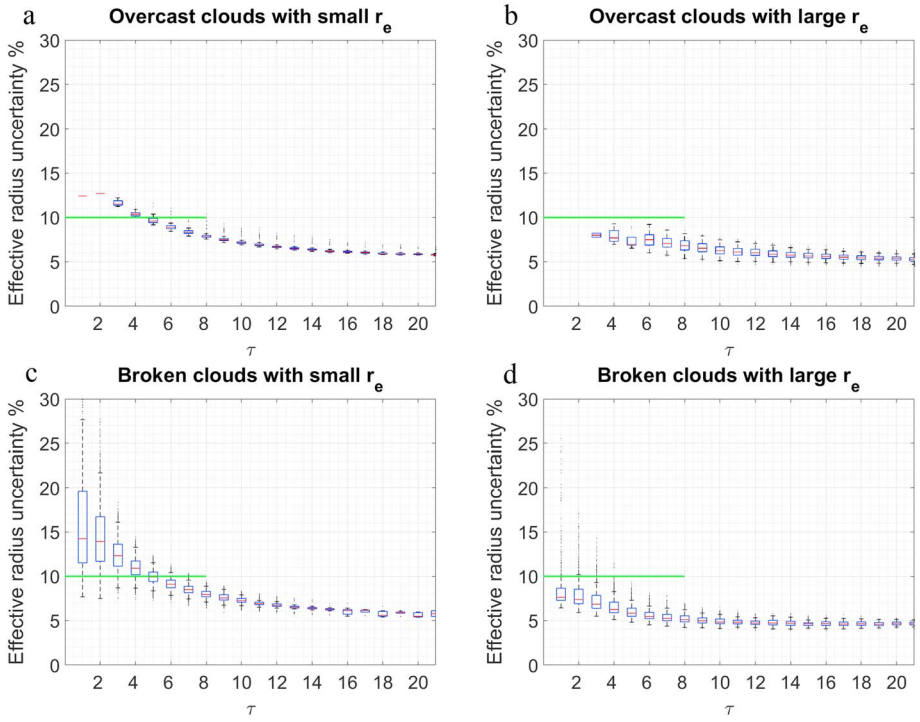

Figure 3. Relationship between cloud optical thickness (τ) and effective radius uncertainty (in %). The τ bin size is one. The horizontal dividers of the bars are median values.

3.4. Selecting Only Single-Layer Clouds

Only single-layer water clouds are analyzed in this study, which can be differentiated from multilayer clouds by virtue of MODIS multichannel measurements. The MODIS algorithm uses the difference between retrieved above-cloud precipitable water amounts from the 0.94 μm water vapor band and from CO_2 slicing, and cloud top height, together with additional tests to provide information about multilayered clouds (Chang & Li, 2005a, 2005b; Wind et al., 2010).

3.5. Selecting Reliable Cloud Properties

Because the reliability of retrieved cloud properties starts deteriorating with increasing SZA (Grosvenor & Wood, 2014), retrievals done when the SZA is greater than 65° are excluded in this study.

In summary, we rejected pixels that have (1) an r_e uncertainty at 2.1 μm greater than 10%, (2) SZA greater than 65°, (3) ice particles, and (4) more than one cloud layer.

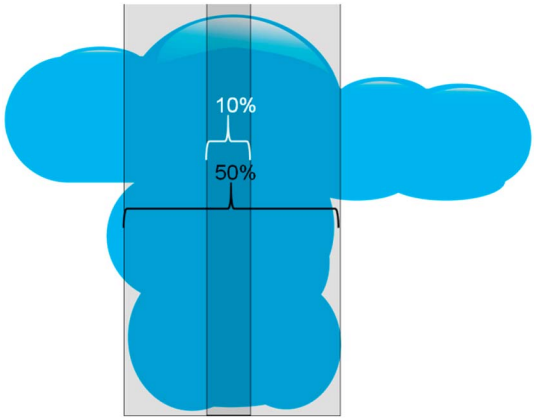

Figure 4. Illustration of a cloud with an anvil below the inversion. The upper median of τ in the cloudy area includes most of the convective elements. The highest 10% contains the cores of the convective elements.

4. Evaluating the Retrieval Biases of N_d Under Different Conditions

The retrieval bias is evaluated with reference to the retrieval for plane-parallel homogeneous clouds. To test it in a real cloud field, we selected an area of marine stratocumulus clouds with full cloud cover and an adjacent area with open cells in the southeast Pacific Ocean to the west of South America. As the r_e distribution (Figure 5a) shows, Area1 and Area2 are adjacent to each other with sharp transitions from overcast clouds to broken clouds. We can see the large contrast in MODIS-retrieved N_d (Figure 5b) between these two areas after filtering pixels according to the criteria given in section 3. The simple average of N_d ($N_{d\_average}$) for the overcast clouds area is 83 drops/cm^3, which is nearly 5 times that of the broken cloud field (17 drops/cm^3). The smaller N_d for broken clouds leads to large

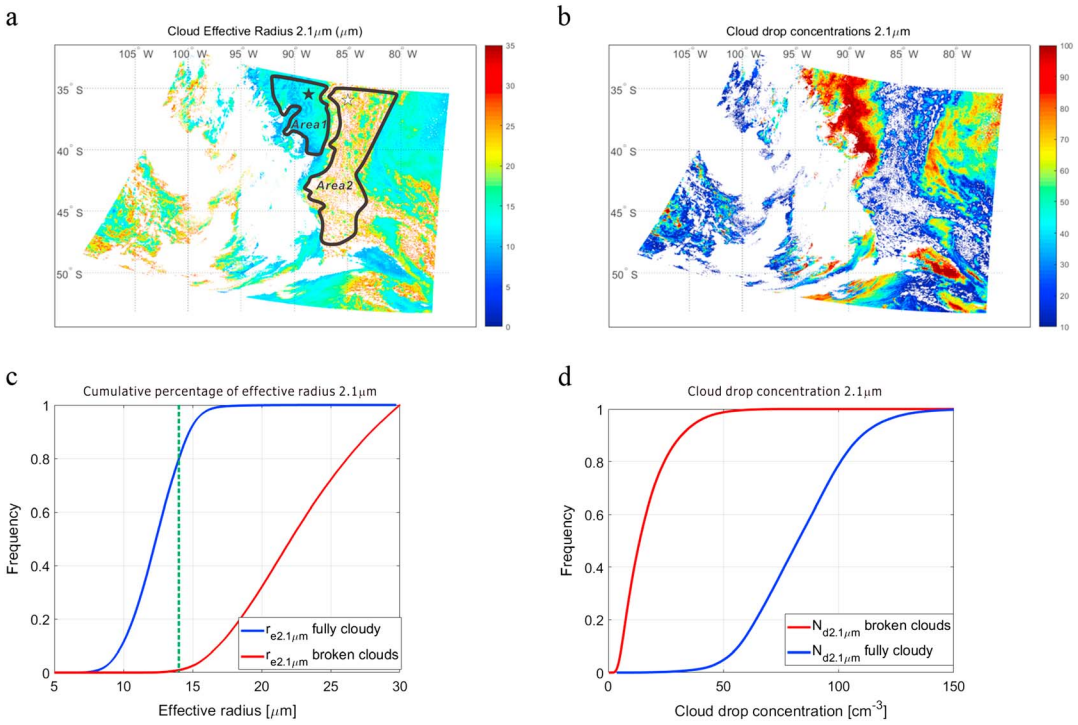

Figure 5. (a) Distribution of MODIS-retrieved r_e on 1 November 2015 at 1600 (UTC). The white (35.47°S, 83.34°W) and black (35.07°S, 89.95°W) stars are the areas that are magnified in Figures 6 and 7, respectively. (b) Retrieved N_d before the application of any selection criteria. (c) The cumulative percentage of r_e after the filtering criteria is applied. (d) The cumulative percentage of N_d after the filtering criteria is applied. The green dashed line in (c) shows the r_e threshold of precipitation (14 μm).

r_e (Figure 5c), which is about double the r_e of the overcast cloud area. Clouds breakup mainly because they precipitate (Rosenfeld et al., 2006), as indicated by r_e much larger than 14 μm, the r_e threshold of precipitation (the green dashed line in Figure 5c; Andreae et al., 2004; Rosenfeld, 1999; Rosenfeld & Gutman, 1994; Rosenfeld & Woodley, 2003; Rosenfeld et al., 2012; Suzuki et al., 2010). The precipitation threshold is mostly not reached in the overcast cloud area, as indicated by the percentage of r_e smaller than 14 μm (80%).

According to the Twomey effect, τ increases with more numerous but smaller cloud droplets in a cloud with the same LWP (Twomey, 1959). Figure 6 is a magnified view of the area shown by white star in Figure 5a. The center parts of the clouds are brighter at 0.64 μm than their borders (Figure 6a). This means that τ is larger in the centers of the clouds. The uncertainty in r_e (Figure 6c) is larger near the cloud edges where clouds are broken, causing a positive bias in r_e (Vant-Hull et al., 2007). The large r_e near the borders, mostly greater than 20 μm, shows this. With smaller r_e and larger τ at the centers of the clouds, the retrieved N_d is much larger at the centers than at the borders of the clouds (Figure 6d).

Figure 7 shows a similar analysis but for the area shown by the black star in Figure 5a. Compared to the broken clouds, the overcast clouds are mostly brighter with some dark bands (Figure 7a). The corresponding r_e is also smaller within the dark stripes (Figure 7b). This can be explained by the dynamics of closed cells. It is possible that the darker borders of the cells are dominated by downward motion, which compensates for the ascending cloudy air in the bright center of the scene (Rosenfeld et al., 2006). The droplets of broken clouds in descending air evaporate and the clouds become optically thin, appearing darker. This results in reduced r_e. Retrieval errors are also a likely cause, as shown by the large r_e retrieval uncertainties (Figure 7c). The retrieved N_d of the overcast cloud area varies from 80 to 130/cm^3 (Figure 7d). The darker parts of the clouds have larger indicated N_d since N_d is more sensitive to the relative changes in r_e than in τ according to equation (1).

Parts of both broken and overcast clouds have high uncertainties, but they affect the retrieved N_d differently. For broken clouds, the highest uncertainties occur at cloud edges where r_e is mostly greater than 20 μm and τ is about 5–10. At the cloud center, r_e is about 14–20 μm and τ is about 10–25, with some pixels even reaching

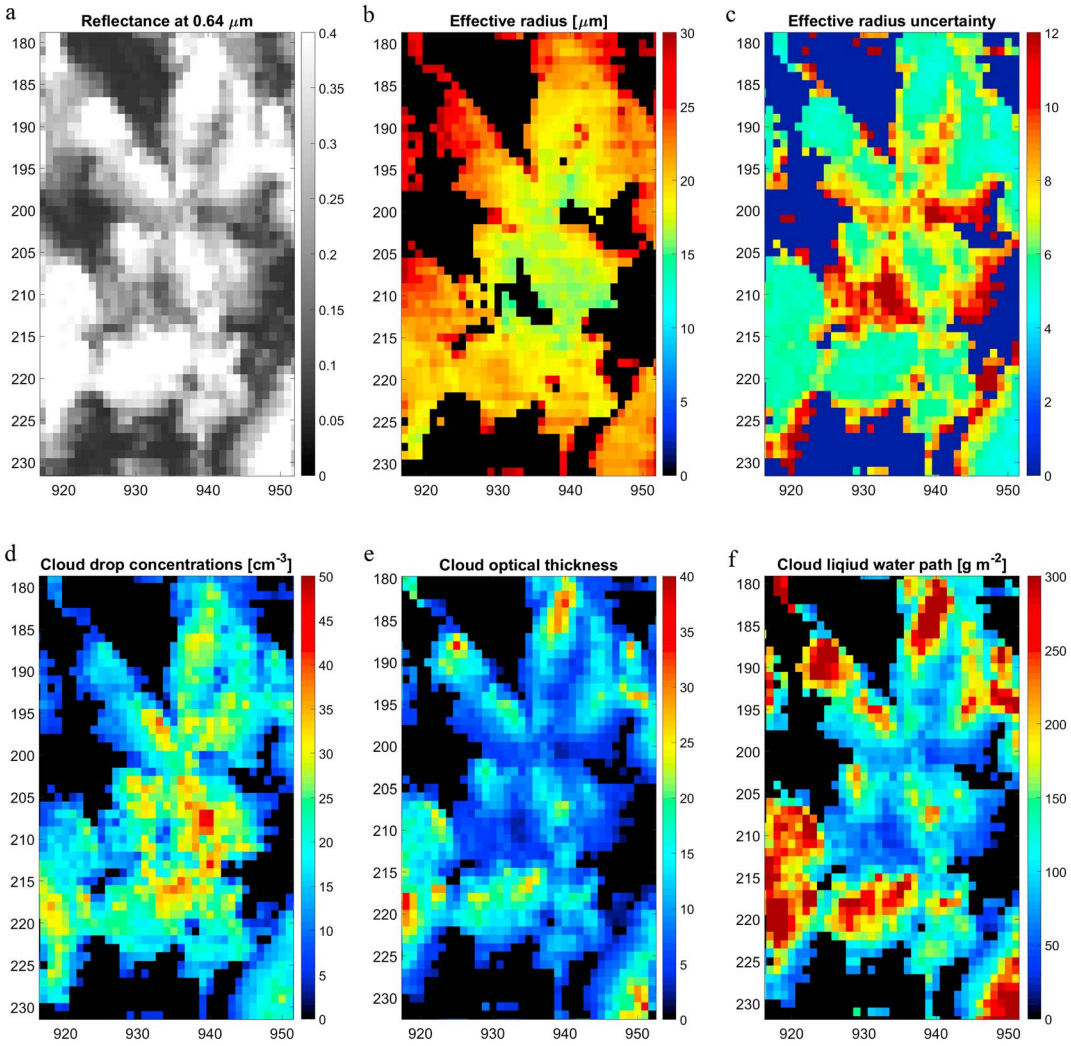

Figure 6. The fine structure of broken clouds. The six panels show magnified views of different cloud properties within Area2 (i.e., white star) in Figure 5a: (a) visible reflectance at 0.64 μm, (b) effective radius at 2.1 μm, (c) effective radius uncertainty at 2.1 μm, d cloud drop concentration, e τ, and f LWP.

40. As a result, the retrieved N_d in the center (19–47 drops/cm^3) is several times larger than the N_d at the cloud edge (5–10 drops/cm^3).

This relationship is reversed in the overcast area (indicated by the black star). Both r_e and τ decrease toward the darker parts of the clouds, but in this case, the retrieved N_d is larger than the N_d of the brighter cloud centers. There is no presently known process that would do this in the descending branch of closed cells, which is marked by the darker borders between the adjacent cloud patches. Therefore, it is likely an artifact. We hypothesize that this would be the case if the cloud top r_e diminishes faster than the r_e lower in the cloud due to enhanced mixing with descending dry air there. The error, if true, indicates that an increase in N_d occurs because N_d is more sensitive to changes in r_e than to changes in τ. According to equation (1), the sensitivity of uncertainties in N_d is about 5 times larger due to the uncertainty in r_e rather than to the uncertainty in τ, due to the form of the functional dependence of N_d on τ and r_e (5 = [5/2]/[1/2]).

The partial pixel filling bias is expected to become larger for smaller cloud fractions (CFs) in the scene. According to Figure 6e, the cores of the broken clouds have larger τ than their fringes where the bias due to partial pixel filling is likely greater. Therefore, the bias is expected to be smaller for higher percentiles of τ.

The bias is expected to be smaller for pixels that are fully embedded within other cloudy pixels. This is defined in our analysis as cloudy pixels whose eight neighboring pixels are also cloudy. Therefore, the central pixel is least likely to have partial cloud filling. Relative biases were estimated for 199,595 scenes

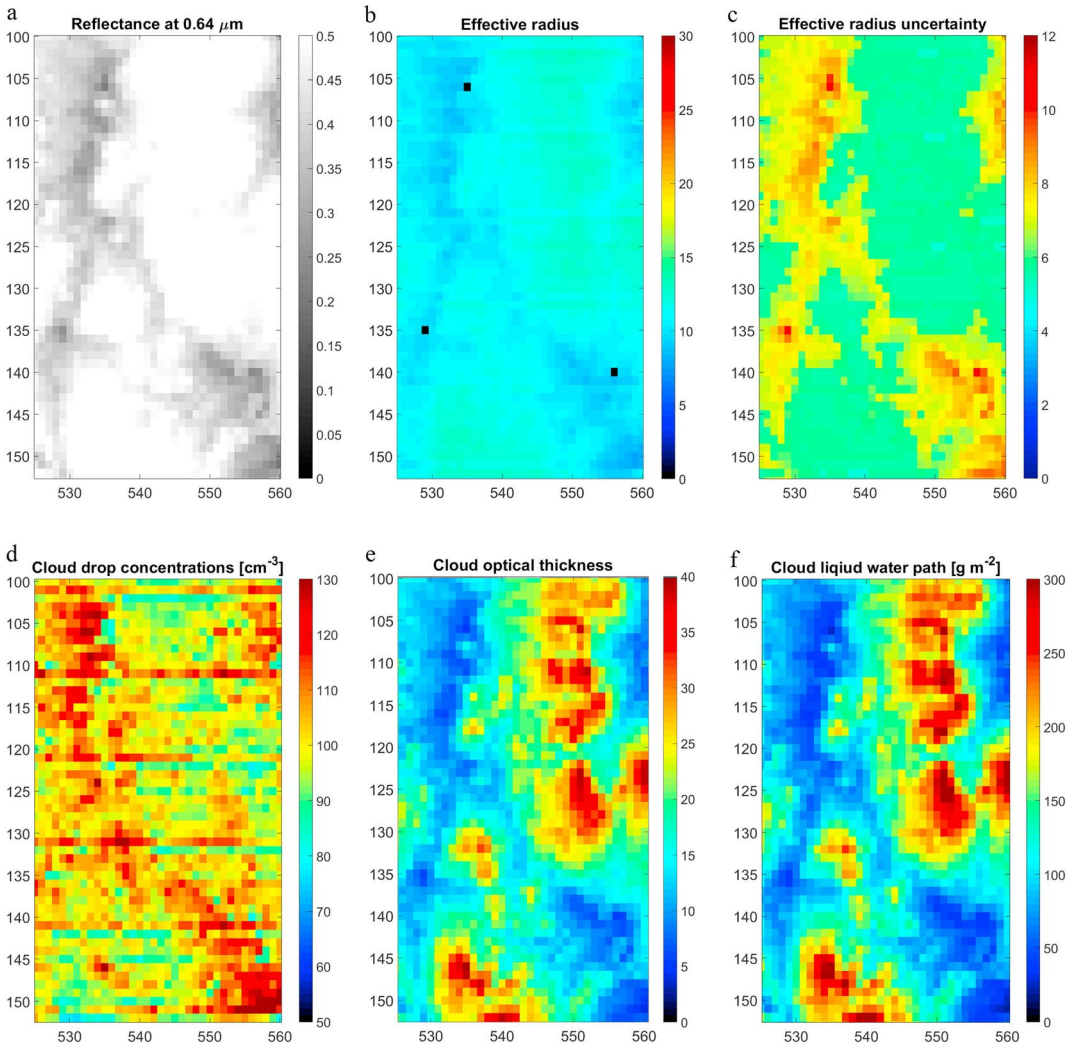

Figure 7. Same as Figure 6 but for the black star in Area1 of Figure 5a, which is an overcast cloud field.

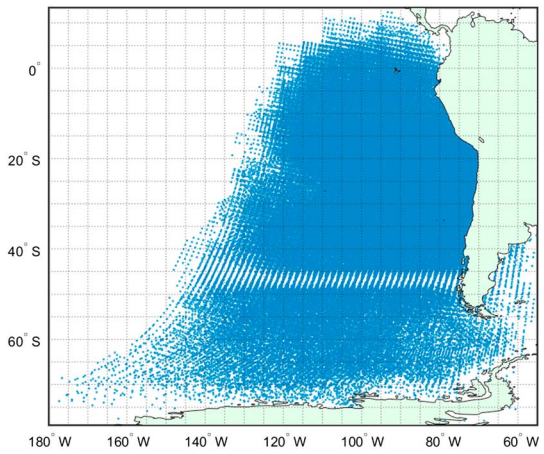

Figure 8. Distribution of the scenes analyzed in this study. Only the center location of each scene is shown due to the large number of scenes and the overlapping of MODIS Terra granules.

in the southern Pacific Ocean containing single-layer liquid-water only shallow marine clouds. The scenes were collected from November to the next February of 2015 and 2016, and over the latitude range of 12°N–78°S and the longitude range of 65°W–177°W (Figure 8).

Convective cores are closest to adiabatic and thus less subject to retrieval biases. Convective cores have the highest LWP compared to the surrounding clouds. Therefore, they can be identified by taking the upper percentiles of τ. A larger τ is also less subject to surface contamination for values of $\tau > \sim 8$ (Rosenfeld et al., 2004). The least bias is expected for overcast pixels. In broken clouds, the fully embedded cloudy pixels are most similar to the situation of full cloud cover.

Here we examine the relative bias of N_d retrieved by various methods with respect to fully embedded pixels. When the cloud cover becomes smaller, clouds become more broken and the bias is expected to increase with respect to full cloud cover. Similarly, for the same CF, the bias is expected to increase in the following order: embedded pixels with the highest 10% of τ, pixels with the highest 10% of τ but not embedded, pixels with the highest 50% of τ, and finally all cloudy pixels (simple average).

Table 2
Cloud Fraction Categories

Categories	Cloud Fraction Range
1	$0 < CF \leq 0.1$
2	$0.1 < CF \leq 0.2$
3	$0.2 < CF \leq 0.3$
4	$0.3 < CF \leq 0.4$
5	$0.4 < CF \leq 0.5$
6	$0.5 < CF \leq 0.6$
7	$0.6 < CF \leq 0.7$
8	$0.7 < CF \leq 0.8$
9	$0.8 < CF \leq 0.99$
10	$0.99 < CF \leq 1$

This order of bias forms the foundation for a systematic evaluation. In preparation for this evaluation, the following parameters were computed for each scene: CF, $N_{d\_average}$, N_{d50}, N_{d90}, and $N_{d90\_embedded}$. Here the average of N_d is calculated as the average of all N_d values, N_{d50} and N_{d90} are calculated using pixels with τ_{50} and τ_{90}, respectively, and $N_{d90\_embedded}$ is calculated using those pixels embedded with other cloudy pixels with τ_{90}. The $N_{d90\_embedded}$ is expected to have the least bias due to partial pixel filling. We categorize all scenes into different CF categories (Table 2), from nearly cloudless ($CF < 0.1$) to overcast clouds because the greater the cloud cover, the more homogeneous the cloud becomes and the smaller is the bias in N_d.

The ratios of the various estimates of N_d to the least biased N_d as a function of CF is shown in Figure 9. The ratio of $N_{d\_average}$ to $N_{d90\_embedded}$ in logarithmic space ranges from −0.117 to −0.038 (linear ratios of 0.76–0.92) as CF increases from 0.05 to 1. The ratio approaches 0.92 as CF approaches 1 (Figure 9a). Using only τ_{50} to calculate N_{d50} does not make much difference with respect to the bias in N_d whose ratio ranges from −0.093 to −0.027 (linear ratios of 0.81–0.93; Figure 9b). Finally, testing the relative bias between N_{d90} and $N_{d90\_embedded}$ (Figure 9c) shows a

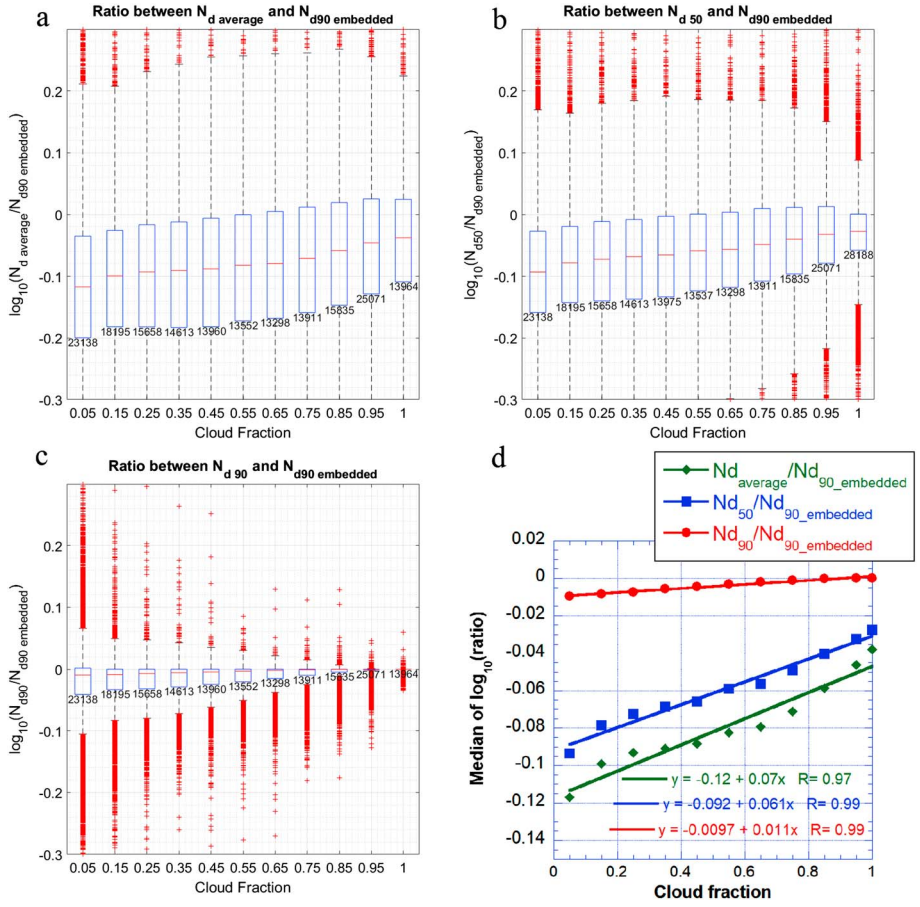

Figure 9. Ratios of N_d retrieved for different percentiles of τ to $N_{d90\_embedded}$ as a function of the mean CF for each cloud fraction category (Table 2): (a) $N_{d\_average}/N_{d90\_embedded}$, (b) $N_{d50}/N_{d90\_embedded}$, and (c) $N_{d90}/N_{d90\_embedded}$. All data for each category are shown as box plots where the red horizontal line in the box is the median, the upper boundary of the box is the 75th percentile, and the lower boundary of the box is the 25th percentile. The number of cases in each category is written below each box. The dashed lines extending vertically from the boxes indicate variability outside the upper and lower quartiles, which starts at the minimum value and ends at the maximum value. The ordinate is the log of the N_d ratio. (d) The median of the log of different N_d ratios as a function of CF.

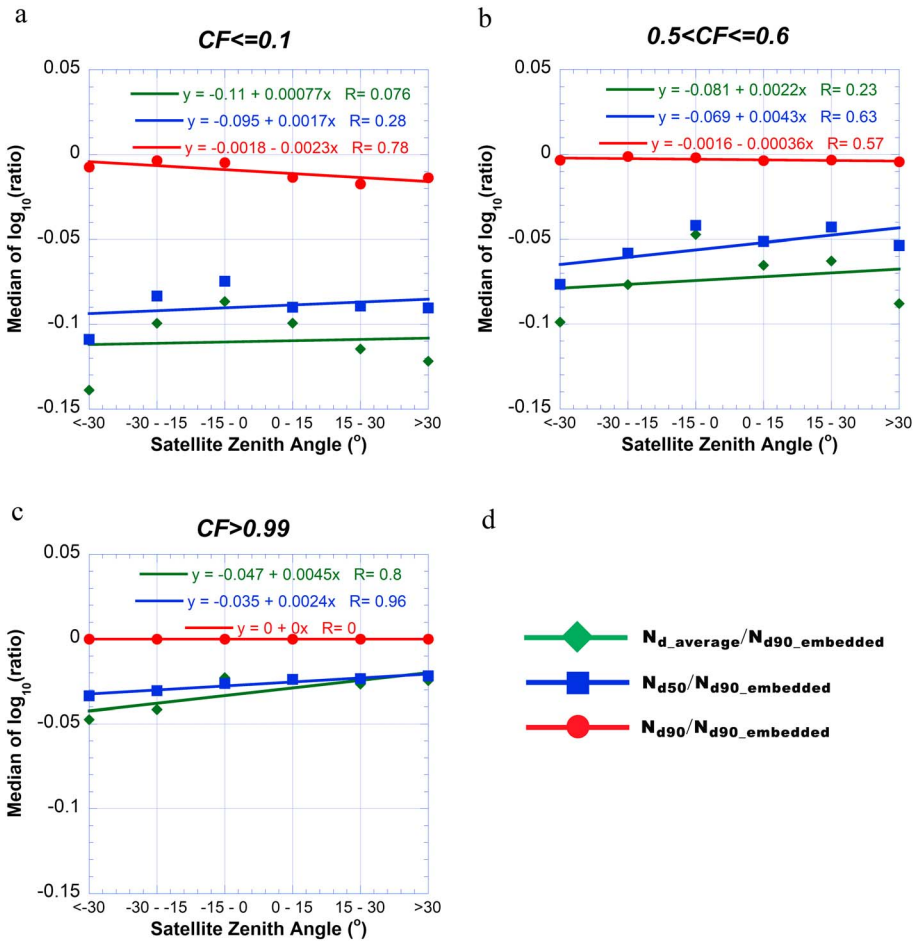

Figure 10. Same as Figure 9d but categorized according to satellite zenith angle for cases where (a) CF ≦ 0.1, (b) 0.5 < CF ≦ 0.6, and (c) CF > 0.99.

maximum negative bias of −0.0096 (0.98 in linear space) for the smallest CF. This is where the strongest effect of partial pixel filling is expected. The N_d ratio bias analysis is summarized in Figure 9d, which shows the medians of the various N_d ratios as a function of CF. Biases of N_{d90} already lead to a bias <2% with respect to $N_{d90\_embedded}$. We conclude that using N_{d90} is suitable for obtaining N_d from MODIS data that are representative of $N_{d90\_embedded}$ and thus cloudy pixels that are completely surrounded by other cloudy pixels, which may potentially be prone to less bias. We argue that this also serves the objectives of retrieving N_d that is most closely related to aerosols below cloud bases and that satisfies most closely the adiabatic assumption underlying the retrieval of N_d.

5. Other Factors That May Affect N_d Retrievals

The retrieval bias of r_e may be caused by the three-dimensional geometry of clouds (Vant-Hull et al., 2007), but the effect is likely small for stratocumulus because their tops are relatively flat (Marshak et al., 2006). In theory, the retrieved r_e from the shadowed parts of clouds is positively biased and the bias can become negative in the illuminated parts due to the satellite and Sun relative geometries. To test this effect on N_d retrievals, the N_d ratio was categorized into different satellite viewing zenith angle groups from the shadowed side (west of the satellite nadir for the Terra morning orbit) to the illuminated side (east of the satellite nadir) for a given cloud cover range. If the N_d bias is dominated by the cloud three-dimensional geometry effect, the N_d ratio should increase at a constant rate when the satellite viewing zenith angle changes from the shadowed side to the illuminated side. Figure 10a shows that the ratios of $N_{d\_average}$, N_{d50}, and N_{d90} to $N_{d90\_embedded}$ do not increase constantly when CF ≦ 0.1. As the cloud cover increases,

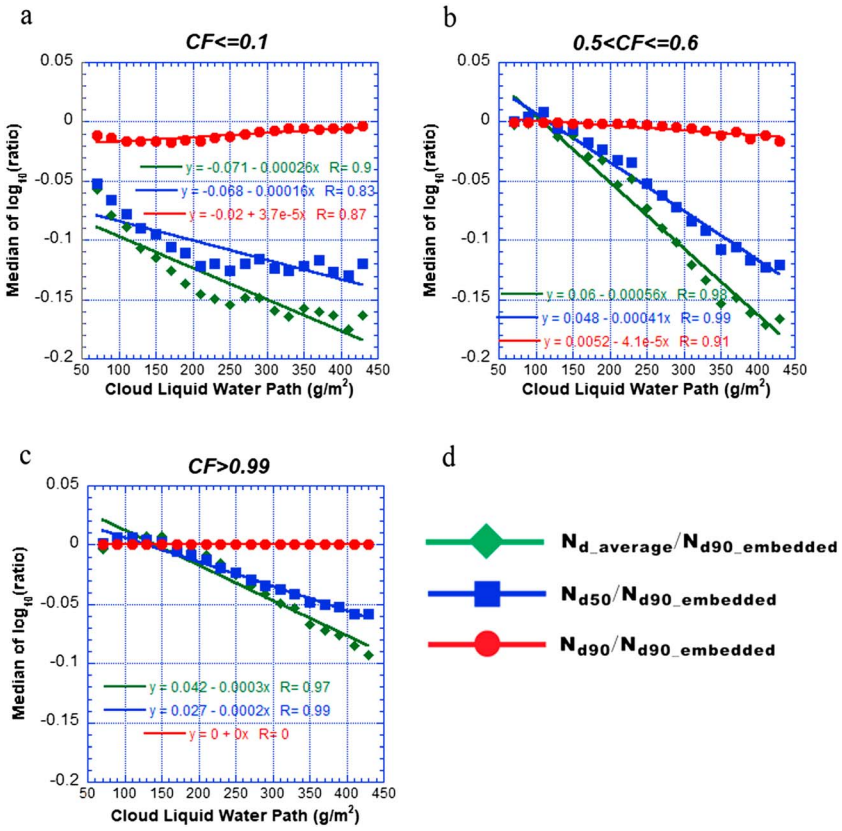

Figure 11. Same as Figure 10 but categorized according to cloud LWP for cases where (a) CF $\leqq$ 0.1, (b) 0.5 $<$ CF $\leqq$ 0.6, and (c) CF $>$ 0.99.

the different N_d ratios also do not increase from the shadowed side to the illuminated side (Figures 10b and 10c). However, the ratio becomes closer to 1 when using the upper percentiles of τ to calculate N_d, especially for those pixels that have τ greater than τ_{90}. The difference between the ratios of the various percentiles is much larger than the likely differences due to changes in satellite viewing zenith angle. Since the different percentiles mainly reflect the effect of pixel filling, whereas the satellite viewing zenith angle mainly reflects the three-dimensional effect, results suggest that partially filled pixels are the primary cause for the r_e bias. This suggests that partially filled pixels dominate the r_e bias and further influence the retrieved N_d in shallow clouds.

Figure 11 shows the relative biases as a function of cloud LWP for different CF. The $N_{d\_average}$ and N_{d50} biases are larger for small CF at a given LWP level, which means that the smaller the CF, the less homogenous are the clouds. The bias also increases with increasing LWP. Clouds with small CFs and higher LWPs appear to be deeper, more convective, and closer to the properties of convective cores. But when they meet the inversion in the upper atmosphere, they spread to form a cloud anvil. This explains why $N_{d\_average}$ and N_{d50} have large biases and why this bias decreases as CF increases, that is, as clouds become more homogenous. Pixels with the highest 10% τ (N_{d90}) have the smallest biases, which are less than 2% for all LWPs and CFs considered.

In summary, the portion of clouds with the highest LWP should be closest to adiabatic, and therefore, the N_d retrievals with the adiabatic assumption would be closest to the actual cloud conditions. On the other hand, clouds with higher LWPs are deeper, more convective, and therefore tend to have a greater inhomogeneity. In addition, the tops of convective clouds tend to spread under inversions into much thinner-layered clouds, contributing to cloud inhomogeneity even in overcast scenes. Moreover, LWP retrievals also use r_e, so using LWP would affect the N_d retrievals. Therefore, we need to use the τ greater than the 90th percentile of τ to represent the convective core even for clouds with large LWPs.

Table 3
Different Types of Calculated N_d Applied to the Overcast Clouds and Broken Cloud Areas

	Overcast clouds		Broken clouds	
Type of N_d	N_d (cm^{-3})	Number of pixels	N_d (cm^{-3})	Number of pixels
$N_{d\_high\_uncertainty}$	113	3,190	11	6,653
$N_{d\_average}$	101	214,142	21	190,945
N_{d50}	96	108,697	28	99,476
N_{d90}	98	21,736	35	19,924
$N_{d90\_embedded}$	98	21,736	38	17,200

6. Application to Test Cases

Various ways of calculating N_d were applied to the overcast cloud (Area1) and broken cloud (Area2) areas shown in Figure 5a. The calculated N_d and the number of pixels used in each calculation are summarized in Table 3.

In the overcast area, N_d with a high uncertainty (i.e., the r_e uncertainty at 2.1 μm greater than 10%) is greater than that of the most reliable $Nd_{90\_embedded}$. One possible reason is that near the descending branches of the clouds in the closed cells of marine stratocumulus, evaporation at the cloud top reduces r_e more than in the deeper portions of the clouds within the satellite view. Another possible reason is that the N_d retrieval starts to break down in these downdraft regions, for example, the assumption of cloud adiabaticity becomes invalid, or perhaps N_d is not constant throughout the cloud. These cloud pixels have higher uncertainties because the evaporating clouds start to break up and become thinner and less homogeneous. Besides $N_{d\_high\_uncertainty}$, $N_{d\_average}$, N_{d50}, N_{d90}, and $N_{d90\_embedded}$ have a similar N_d because the overcast cloud area is mostly homogeneous, which is close to the assumption of an adiabatic cloud. This homogeneity maximizes the likelihood that any part of the cloud can represent convective elements. The full cloud coverage also reduces the possibility of partial pixel filling.

There are large differences between the results from the broken cloud area and the overcast cloud area as Table 3 shows. First, the number of high uncertainty pixels for the broken cloud case is twice that of the overcast cloud case because there are more cloud edges. High-uncertainty N_d for the broken cloud case has the smallest number of N_d, which are mostly located at the cloud edge. The low N_d could be an actual reduction in N_d in the low optical depth region due to cloud evaporation, or lower updrafts toward cloud edges compared with the updraft cores. A bias due to partial pixel filling can cause an overestimated r_e, which leads to an underestimated N_d. The N_d almost doubles from 11 to 21/cm^3 for pixels that are not designated with high uncertainty, as $N_{d\_average}$ shows. The retrieved N_d increases to 28/cm^3 when the τ percentile is increased to 50, which amounts to an increase of 33% compared to $N_{d\_average}$. A further increase of τ to τ_{90} increases the retrieved N_d by an additional 25% to 35/cm^3. In all, according to Table 3, the partially filled cloudy pixels are marked with high uncertainty and have less than one third of the N_d of the convective core in partially cloudy scenes. The number of pixels with $\tau > \tau_{90}$ is decreased by about 4 times with respect to $\tau > \tau_{50}$ because they are mostly close to the convective cores. This suggests that N_{d50} is still affected by partial pixel filling. N_{d90} and $N_{d90\_embedded}$ differ minimally, which suggests that N_{d90} is not affected by partial pixel filling very much. Therefore, using a high percentile of τ ($\tau > \tau_{90}$) can minimize the bias of partially filled pixels effectively in N_d retrievals for broken clouds. We conclude that N_{d90} is sufficient to represent the N_d of convective cores.

7. Summary and Conclusions

We have shown that the N_d of broken clouds over oceans is less than a factor of 3 on average, compared to nearby homogeneous clouds where retrieval artifacts are least significant. An unknown part of this difference may be attributed to a physical reduction of N_d in the peripheral clouds compared with convective cores.

Partial pixel filling, cloud inhomogeneity, and τ all affect retrievals of N_d. Such biases can likely be minimized by focusing the retrievals on the most reflective 10% of MODIS cloudy pixels (N_{d90}), which are those pixels with the highest 10% of τ for a given scene. This methodology provides the N_d of the convective cores of clouds, which are likely the closest to adiabatic. Because retrieving N_d assumes an adiabatic cloud vertical profile, N_{d90} is also likely to be minimally biased due to deviations from the adiabatic assumption. N_{d90} in the convective cores also reflects best the effects of boundary layer aerosols on cloud microstructure.

There is no evident bias in N_d due to variations in satellite viewing geometry because marine shallow clouds generally have flat tops compared to convective clouds. The average N_d, $N_{d\_average}$, mixes convective cores with their spreading tops and decaying portions, which may violate the assumptions of the underlying N_d retrieval.

Most importantly, N_{d90} is representative of the N_d from the most reflective 10% of pixels of a given scene that are also completely surrounded by other cloudy pixels, which likely represent the ideal conditions for MODIS retrievals. N_{d90} likely represents best the microphysical response of clouds to the variability in CCN and W_b. Therefore, N_{d90} is likely to be the most suitable parameter for studying satellite-retrieved aerosol-cloud interactions within the framework of passive instrument N_d estimates based upon r_e and τ.

Author Contributions

Y. Z. and D. R. designed the research; Y. Z. and D. R. carried out analyses and wrote the manuscript. D. R. and Z. L. discussed the results.

Acknowledgments
We thank the anonymous reviewers for their helpful suggestions. This research was supported by the Joint NSFC-ISF Research Program (41561144004) and jointly funded by the National Natural Science Foundation of China and the Israel Science Foundation, the National Natural Science Foundation of China (41575136 and 91544217), NASA (NNX16AN61G), and the China Special Fund for Meteorological Research in the Public Interest (GYHY201306005). The MODIS L2 cloud product data in this study are obtained from the National Aeronautics and Space Administration (https://search.earthdata.nasa.gov).

References

Albrecht, B. A. (1989). Aerosols, cloud microphysics, and fractional cloudiness. *Science*, *245*(4923), 1227–1230. https://doi.org/10.1126/science.245.4923.1227

Andreae, M. O. (2009). Correlation between cloud condensation nuclei concentration and aerosol optical thickness in remote and polluted regions. *Atmospheric Chemistry and Physics*, *9*(2), 543–556. https://doi.org/10.5194/acp-9-543-2009

Andreae, M. O., Rosenfeld, D., Artaxo, P., Costa, A. A., Frank, G. P., Longo, K. M., & Silva-Dias, M. A. (2004). Smoking rain clouds over the Amazon. *Science*, *303*(5662), 1337–1342. https://doi.org/10.1126/science.1092779

Baum, B. A., Kratz, D. P., Yang, P., Ou, S. C., Hu, Y., Soulen, P. F., & Tsay, S. C. (2000). Remote sensing of cloud properties using MODIS airborne simulator imagery during SUCCESS. 1. Data and models. *Journal of Geophysical Research*, *105*(D9), 11,767–11,780. https://doi.org/10.1029/1999JD901089

Baum, B. A., Menzel, W. P., Frey, R. A., Tobin, D. C., Holz, R. E., Ackerman, S. A., et al. (2012). MODIS cloud-top property refinements for Collection 6. *Journal of Applied Meteorology and Climatology*, *51*(6), 1145–1163. https://doi.org/10.1175/JAMC-D-11-0203.1

Bennartz, R. (2007). Global assessment of marine boundary layer cloud droplet number concentration from satellite. *Journal of Geophysical Research*, *112*, D02201. https://doi.org/10.1029/2006JD007547

Bennartz, R., & Rausch, J. (2017). Global and regional estimates of warm cloud droplet number concentration based on 13 years of AQUA-MODIS observations. *Atmospheric Chemistry and Physics*, *17*(16), 9815–9836. https://doi.org/10.5194/acp-17-9815-2017

Brenguier, J. L., Pawlowska, H., Schuller, L., Preusker, R., Fischer, J., & Fouquart, Y. (2000). Radiative properties of boundary layer clouds: Droplet effective radius versus number concentration. *Journal of the Atmospheric Sciences*, *57*(6), 803–821. https://doi.org/10.1175/1520-0469(2000)057<0803:RPOBLC>2.0.CO;2

Chang, F. L., & Li, Z. (2002). Estimating the vertical variation of cloud droplet effective radius using multispectral near-infrared satellite measurements. *Journal of Geophysical Research*, *107*(D15), 4257. https://doi.org/10.1029/2001jd000766

Chang, F. L., & Li, Z. (2003). Retrieving vertical profiles of water-cloud droplet effective radius: Algorithm modification and preliminary application. *Journal of Geophysical Research*, *108*(D24), 4763. https://doi.org/10.1029/2003JD003906

Chang, F. L., & Li, Z. (2005a). A near-global climatology of single-layer and overlapped clouds and their optical properties retrieved from Terra/MODIS data using a new algorithm. *Journal of Climate*, *18*(22), 4752–4771. https://doi.org/10.1175/JCLI3553.1

Chang, F. L., & Li, Z. (2005b). A new method for detection of cirrus overlapping water clouds and determination of their optical properties. *Journal of the Atmospheric Sciences*, *62*(11), 3993–4009. https://doi.org/10.1175/JAS3578.1

Chen, R., Chang, F. L., Li, Z., Ferraro, R., & Weng, F. (2007). Impact of the vertical variation of cloud droplet size on the estimation of cloud liquid water path and rain detection. *Journal of the Atmospheric Sciences*, *64*(11), 3843–3853. https://doi.org/10.1175/2007JAS2126.1

Chen, R., Li, Z., Kuligowski, R. J., Ferraro, R., & Weng, F. (2011). A study of warm rain detection using A-Train satellite data. *Geophysical Research Letters*, *38*, L04804. https://doi.org/10.1029/2010GL046217

Coakley, J. A. Jr., Friedman, M. A., & Tahnk, W. R. (2005). Retrieval of cloud properties for partly cloudy imager pixels. *Journal of Atmospheric and Oceanic Technology*, *22*(1), 3–17. https://doi.org/10.1175/JTECH-1681.1

Freud, E., & Rosenfeld, D. (2012). Linear relation between convective cloud drop number concentration and depth for rain initiation. *Journal of Geophysical Research*, *117*, D02207. https://doi.org/10.1029/2011JD016457

Freud, E., Rosenfeld, D., & Kulkarni, J. (2011). Resolving both entrainment-mixing and number of activated CCN in deep convective clouds. *Atmospheric Chemistry and Physics*, *11*(24), 12,887–12,900. https://doi.org/10.5194/acp-11-12887-2011

Gerber, H. (1996). Microphysics of marine stratocumulus clouds with two drizzle modes. *Journal of the Atmospheric Sciences*, *53*(12), 1649–1662. https://doi.org/10.1175/1520-0469(1996)053<1649:MOMSCW>2.0.CO;2

Goren, T., & Rosenfeld, D. (2014). Decomposing aerosol cloud radiative effects into cloud cover, liquid water path and Twomey components in marine stratocumulus. *Atmospheric Research*, *138*, 378–393. https://doi.org/10.1016/j.atmosres.2013.12.008

Goren, T., & Rosenfeld, D. (2015). Extensive closed cell marine stratocumulus downwind of Europe—A large aerosol cloud mediated radiative effect or forcing? *Journal of Geophysical Research: Atmospheres*, *120*, 6098–6116. https://doi.org/10.1002/2015JD023176

Grosvenor, D. P., & Wood, R. (2014). The effect of solar zenith angle on MODIS cloud optical and microphysical retrievals within marine liquid water clouds. *Atmospheric Chemistry and Physics*, *14*(14), 7291–7321. https://doi.org/10.5194/acp-14-7291-2014

Hayes, C. R., Coakley, J. A., & Tahnk, W. R. (2010). Relationships among properties of marine stratocumulus derived from collocated CALIPSO and MODIS observations. *Journal of Geophysical Research*, *115*, D00H17. https://doi.org/10.1029/2009JD012046

Marchant, B., Platnick, S., Meyer, K., Arnold, G. T., & Riedi, J. (2016). MODIS Collection 6 shortwave-derived cloud phase classification algorithm and comparisons with CALIOP. *Atmospheric Measurement Techniques*, *9*(4), 1587–1599. https://doi.org/10.5194/amt-9-1587-2016

Marshak, A., Platnick, S., Varnai, T., Wen, G., & Cahalan, R. F. (2006). Impact of three-dimensional radiative effects on satellite retrievals of cloud droplet sizes. *Journal of Geophysical Research*, *111*, D09207. https://doi.org/10.1029/2005jd006686

Min, Q., Joseph, E., Lin, Y., Min, L., Yin, B., Daum, P. H., et al. (2012). Comparison of MODIS cloud microphysical properties with in-situ measurements over the Southeast Pacific. *Atmospheric Chemistry and Physics*, *12*(23), 11,261–11,273. https://doi.org/10.5194/acp-12-11261-2012

Nakajima, T., & King, M. D. (1990). Determination of the optical thickness and effective particle radius of clouds from reflected solar radiation measurements. Part I: Theory. *Journal of the Atmospheric Sciences*, *47*(15), 1878–1893. https://doi.org/10.1175/1520-0469(1990)047<1878:DOTOTA>2.0.CO;2

Nakajima, T. Y., Suzuki, K., & Stephens, G. L. (2010a). Droplet growth in warm water clouds observed by the A-Train. Part I: Sensitivity analysis of the MODIS-derived cloud droplet sizes. *Journal of the Atmospheric Sciences*, *67*(6), 1884–1896. https://doi.org/10.1175/2009JAS3280.1

Nakajima, T. Y., Suzuki, K., & Stephens, G. L. (2010b). Droplet growth in warm water clouds observed by the A-Train. Part II: A multisensor view. *Journal of the Atmospheric Sciences*, *67*(6), 1897–1907. https://doi.org/10.1175/2010JAS3276.1

Painemal, D., & Zuidema, P. (2011). Assessment of MODIS cloud effective radius and optical thickness retrievals over the Southeast Pacific with VOCALS-REx in situ measurements. *Journal of Geophysical Research*, 116, D24206. https://doi.org/10.1029/2011JD016155

Pawlowska, H., Brenguier, J., & Burnet, F. (2000). Microphysical properties of stratocumulus clouds. *Atmospheric Research*, *55*(1), 15–33. https://doi.org/10.1016/S0169-8095(00)00054-5

Pinsky, M., Khain, A., Mazin, I., & Korolev, A. (2012). Analytical estimation of droplet concentration at cloud base. *Journal of Geophysical Research*, *117*, D18211. https://doi.org/10.1029/2012JD017753

Platnick, S. (2000). Vertical photon transport in cloud remote sensing problems. *Journal of Geophysical Research*, *105*(D18), 22,919–22,935. https://doi.org/10.1029/2000JD900333

Platnick, S., King, M. D., Meyer, K. G., Wind, G., Amarasinghe, N., Marchant, B., et al. (2015). MODIS cloud optical properties: user guide for the Collection 6 Level-2 MOD06/MYD06 product and associated level-3 datasets. https://modis-images.gsfc.nasa.gov/_docs/C6MOD06OPUserGuide.pdf

Platnick, S., Pincus, R., Wind, B., King, M., Gray, M., & Hubanks, P. (2004). An initial analysis of the pixel-level uncertainties in global MODIS cloud optical thickness and effective particle size retrievals. *Paper presented at Fourth International Asia-Pacific Environmental Remote Sensing Symposium 2004: Remote sensing of the atmosphere, ocean, environment, and space, SPIE*, *5652*, 31. https://doi.org/10.1117/12.578353

Quaas, J., Stevens, B., Stier, P., & Lohmann, U. (2010). Interpreting the cloud cover - aerosol optical depth relationship found in satellite data using a general circulation model. *Atmospheric Chemistry and Physics*, *10*(13), 6129–6135. https://doi.org/10.5194/acp-10-6129-2010

Rangno, A. L., & Hobbs, P. V. (2005). Microstructures and precipitation development in cumulus and small cumulonimbus clouds over the warm pool of the tropical Pacific Ocean. *Quarterly Journal of the Royal Meteorological Society*, *131*(606), 639–673. https://doi.org/10.1256/qj.04.13

Rosenfeld, D. (1999). TRMM observed first direct evidence of smoke from forest fires inhibiting rainfall. *Geophysical Research Letters*, *26*(20), 3105–3108. https://doi.org/10.1029/1999GL006066

Rosenfeld, D., Cattani, E., Melani, S., & Levizzani, V. (2004). Considerations on daylight operation of 1.6-versus 3.7-μm channel on NOAA and Metop satellites. *Bulletin of the American Meteorological Society*, *85*(6), 873–881. https://doi.org/10.1175/BAMS-85-6-873

Rosenfeld, D., & Gutman, G. (1994). Retrieving microphysical properties near the tops of potential rain clouds by multispectral analysis of AVHRR data. *Atmospheric Research*, *34*(1–4), 259–283. https://doi.org/10.1016/0169-8095(94)90096-5

Rosenfeld, D., Kaufman, Y. J., & Koren, I. (2006). Switching cloud cover and dynamical regimes from open to closed Benard cells in response to the suppression of precipitation by aerosols. *Atmospheric Chemistry and Physics*, *6*(9), 2503–2511. https://doi.org/10.5194/acp-6-2503-2006

Rosenfeld, D., Wang, H. L., & Rasch, P. J. (2012). The roles of cloud drop effective radius and LWP in determining rain properties in marine stratocumulus. *Geophysical Research Letters*, *39*, L13801. https://doi.org/10.1029/2012GL052028

Rosenfeld, D., & Woodley, W. (2003). Closing the 50-year circle: From cloud seeding to space and back to climate change through precipitation physics, cloud systems, hurricanes, and the Tropical Rainfall Measuring Mission (TRMM). *Mesoscale Meteorology*, *51*, 59–80.

Rosenfeld, D., Zheng, Y., Hashimshoni, E., Pohlker, M. L., Jefferson, A., Pohlker, C., et al. (2016). Satellite retrieval of cloud condensation nuclei concentrations by using clouds as CCN chambers. *Proceedings of the National Academy of Sciences*, *113*(21), 5828–5834. https://doi.org/10.1073/pnas.1514044113

Seethala, C., & Horvath, A. (2010). Global assessment of AMSR-E and MODIS cloud liquid water path retrievals in warm oceanic clouds. *Journal of Geophysical Research*, *115*, D13202. https://doi.org/10.1029/2009JD012662

Shinozuka, Y., Clarke, A. D., Nenes, A., Jefferson, A., Wood, R., McNaughton, C. S., et al. (2015). The relationship between cloud condensation nuclei (CCN) concentration and light extinction of dried particles: Indications of underlying aerosol processes and implications for satellite-based CCN estimates. *Atmospheric Chemistry and Physics*, *15*(13), 7585–7604. https://doi.org/10.5194/acp-15-7585-2015

Stier, P. (2016). Limitations of passive remote sensing to constrain global cloud condensation nuclei. *Atmospheric Chemistry and Physics*, *16*(10), 6595–6607. https://doi.org/10.5194/acp-16-6595-2016

Suzuki, K., Nakajima, T. Y., & Stephens, G. L. (2010). Particle growth and drop collection efficiency of warm clouds as inferred from joint CloudSat and MODIS observations. *Journal of the Atmospheric Sciences*, *67*(9), 3019–3032. https://doi.org/10.1175/2010JAS3463.1

Szczodrak, M., Austin, P. H., & Krummel, P. B. (2001). Variability of optical depth and effective radius in marine stratocumulus clouds. *Journal of the Atmospheric Sciences*, *58*(19), 2912–2926. https://doi.org/10.1175/1520-0469(2001)058<2912:VOODAE>2.0.CO;2

Twomey, S. (1959). The nuclei of natural cloud formation. Part II: The supersaturation in natural clouds and the variation of cloud droplet concentration. *Pure and Applied Geophysics*, *43*(1), 243–249. https://doi.org/10.1007/BF01993560

Vant-Hull, B., Marshak, A., Remer, L. A., & Li, Z. (2007). The effects of scattering angle and cumulus cloud geometry on satellite retrievals of cloud droplet effective radius. *IEEE Transactions on Geoscience and Remote Sensing*, *45*(4), 1039–1045. https://doi.org/10.1109/TGRS.2006.890416

Wind, G., Platnick, S., King, M. D., Hubanks, P. A., Pavolonis, M. J., Heidinger, A. K., et al. (2010). Multilayer cloud detection with the MODIS near-infrared water vapor absorption band. *Journal of Applied Meteorology and Climatology*, *49*(11), 2315–2333. https://doi.org/10.1175/2010JAMC2364.1

Wolters, E. L. A., Deneke, H. M., van den Hurk, B. J. J. M., Meirink, J. F., & Roebeling, R. A. (2010). Broken and inhomogeneous cloud impact on satellite cloud particle effective radius and cloud-phase retrievals. *Journal of Geophysical Research*, *115*, D10214. https://doi.org/10.1029/2009JD012205

Wood, R., Mecheso, C. R., Bretherton, C. S., Weller, R. A., Huebert, B., Straneo, F., et al. (2011). The VAMOS Ocean-Cloud-Atmosphere-Land Study Regional Experiment (VOCALS-REx): Goals, platforms, and field operations. *Atmospheric Chemistry and Physics*, *11*(2), 627–654. https://doi.org/10.5194/acp-11-627-2011

Zamora, L. M., Kahn, R. A., Eckhardt, S., McComiskey, A., Sawamura, P., Moore, R., & Stohl, A. (2017). Aerosol indirect effects on the nighttime Arctic Ocean surface from thin, predominantly liquid clouds. *Atmospheric Chemistry and Physics*, *17*(12), 7311–7332. https://doi.org/10.5194/acp-17-7311-2017

Zhang, Z. B., Ackerman, A. S., Feingold, G., Platnick, S., Pincus, R., & Xue, H. W. (2012). Effects of cloud horizontal inhomogeneity and drizzle on remote sensing of cloud droplet effective radius: Case studies based on large-eddy simulations. *Journal of Geophysical Research*, *117*, D19208. https://doi.org/10.1029/2012JD017655

Zhang, Z. B., & Platnick, S. (2011). An assessment of differences between cloud effective particle radius retrievals for marine water clouds from three MODIS spectral bands. *Journal of Geophysical Research*, *116*, D20215. https://doi.org/10.1029/2011JD016216

Zheng, Y., Rosenfeld, D., & Li, Z. (2016). Quantifying cloud base updraft speeds of marine stratocumulus from cloud top radiative cooling. *Geophysical Research Letters*, *43*, 11,407–11,413. https://doi.org/10.1002/2016GL071185